Science Advances
AAAS

advances.sciencemag.org/cgi/content/full/4/9/eaat5780/DC1

Supplementary Materials for

High electrical conductivity and carrier mobility in oCVD PEDOT thin films by engineered crystallization and acid treatment

Xiaoxue Wang, Xu Zhang, Lei Sun, Dongwook Lee, Sunghwan Lee, Minghui Wang, Junjie Zhao, Yang Shao-Horn, Mircea Dincă, Tomás Palacios, Karen K. Gleason*

*Corresponding author. Email: kkg@mit.edu

Published 14 September 2018, *Sci. Adv.* **4**, eaat5780 (2018)
DOI: 10.1126/sciadv.aat5780

This PDF file includes:

Section S1. Methods

oCVD synthesis: The oCVD process is described in the Materials and Methods section of the main text. The samples are stored in air-tight desiccators at room temperature. The following measurements are done within 2 weeks of fabrication.

The Seebeck coefficient measurement (36, 37):

Seebeck coefficients of PEDOT samples are measured with a lab-built installation (fig. S2a). At this setup, thermal gradient across each sample is generated by two different Peltier elements. Two individual T-type thermocouples are placed on two different spots of the sample surface to record temperatures at each point and voltage difference at those two points. Mechanical pressure is applied to thermocouples on samples, in order to tightly fix thermocouples at certain positions and provide better electrical contacts between thermocouples and samples. The Seebeck coefficient is measured on PEDOT thin films deposited on Si wafers with 1μm SiO_2 layer.

Room temperature and cryogenic in-plane electrical conductivity measurement: the room temperature electrical sheet resistance measurement is conducted with a standard 4-point probe (Jandal CYL-1.0-100-TC-100-RM3), Keithley 2000 and 2400 multimeters. The film thickness is measured using a Dektak 150 profilometer and Atomic Force Microscope (AFM, Veeco Dimension 3100). The electrical conductivity is calculated by dividing the sheet electrical conductance (multiplicative inverse of sheet resistance) by the film thickness. The cryogenic conductivity measurement is conducted using a probe station (Janis Cryogenics ST-500). The van der Pauw device with gold electrodes (fig. S2b and fig. S2c) was mounted onto the sample chuck of the probe station by a layer of thermal paste (DuPont Krytox) to enable efficient heat transfer. Electrical contacts are made by touching carbon paste on the gold pads with gold-plated tungsten probes, whose positions are controlled by micro-manipulators. The probe station chamber is evacuated to a pressure of 10-5 torr. The temperature is balanced by a heater on the sample chuck and liquid helium, and is controlled by a temperature controller (Scientific Instrument model 9700). Temperature was controlled by the thermal couple and liquid helium. The temperature is increased every 10K from 40K to 300K, with the stabilization time of 30 min at each temperature point. Electrical data is obtained with a Keithley 2450 sourcemeter. The sheet electrical conductance is extracted by the van der Pauw equation (*38*).

Hall effect measurement: The Hall effect measurement set-up is shown in fig. S2d. The magnetic field used is 2800G, and the current applied is 100mA.

Modelling with K-S model: Kang and Snyder established a theoretical model directly derived from Boltzmann transport in order to describe the charge transport in conducting polymers. The model resolves the discrepancy between the predicted and measures values for electrical conductivity and Seebeck coefficient from other popular models such as Mott's VRH model and Mott's mobility edge model. The key equations for K-S model is shown in equation (2-4) in the main text.

In equation (2) of main text, s is a model factor, which is 1 for PEDOT according to the research of Kang and Snyder. s=1 is also validated by the comparison between the calculated value and the experimental value shown in Fig. 3c in the main text. This value, s, is determined by the carrier relaxation time governed by an acoustic-phonon scattering (*9, 39*) or strongly screened ionized impurity scattering

induced by counter-ions(*39*); Additionally, in equations (2) and (3) of main text, $\eta = (E_F - E_t)/k_BT$, where E_F is the Fermi level and E_t is the transport edge. From Kang and Snyder's hypothesis, only carriers with energy above the transport edge E_t contribute to the electrical conductivity; Fermi-Dirac integral $F_i(\eta) = \int_0^\infty \frac{\varepsilon^i}{1+e^{\varepsilon-\eta}} d\varepsilon$ is used in equation (2) and (3).

Figure 3a in the main text shows the Seebeck coefficient at 300K of the samples. With the Seebeck coefficient at room temperature, one can solve $\eta(300K)$ from the equation (3). With the electrical conductivity $\sigma(300K)$ and $\eta(300K)$, we can solve $\sigma_{E0}(300K)$ using equation (2). More details about $\eta(300K)$ calculation and $\sigma_{E0}(300K)$ using the collected data can be found in sections S10 and S11. Furthermore, with $\eta(300K) = (E_F - E_t)/(k_B \times 300K)$, we can calculate $E_F - E_t$, We assume that $E_F - E_t$ does not change with temperature. Using $E_F - E_t$, we can calculate $\eta(T) = (E_F - E_t)/k_BT$ at a given temperature T. In addition, the cryogenic measurement (Fig. 2c in the main text) gives the conductivity $\sigma(T)$ at a series of temperature T. Using the information of $\eta(T)$ and $\sigma(T)$, the transport coefficient $\sigma_{E0}(T)$ can be calculated at various temperature points using equation (2). For instance, Fig. 3b in the main text shows $\sigma_{E0}(300K)$ of different samples deposited at different temperatures, and section S12 shows the $\sigma_{E0}(T)$ vs. T curve for three selected samples.

Transport coefficient σ_{E0} and the carrier mobility μ are related by the equation

$$\mu = \sigma_{E0} \cdot \left(\frac{m^*}{m_e}\right)^{-3/2} \cdot \frac{2\pi^2\hbar^3}{e(2m_e k_B T)^{3/2}} \cdot \frac{sF_{s-1}(\eta)}{F_{1/2}(\eta)} \quad \text{(S1)}$$

where $m*$ is the effective mass of charge carrier, m_e is the mass of an electron, $\hbar$ is reduced Planck constant.

The mobility is calculated with the information of $\sigma_{E0}(T)$ and $\eta(T)$, with the assumptions of $m^* \sim m_e$, $s = 1$(*9, 12*). The calculated mobility at room temperature is plotted in Fig. 3c in the main text, and the $\mu(T)$ vs.T curve is plotted in Fig. 3d.

Characterizations:

Thermogravimetric Analysis (TGA): A Discovery thermogravimetric analyzer from TA Instruments (New Castle, DE) was employed for the TGA measurement. PEDOT films synthesized via oCVD with growth temperature of 220℃ were scraped off the silicon wafer, washed by methanol, followed by drying under vacuum at 35℃ for 2.5 hours before TGA analysis. Approximately 2 mg of PEDOT sample was

used for each measurement. The sample was first equilibrated at 30 °C, followed by isothermal for 1 min, and then the temperature was increased to 450 °C at 20 °C/min. A nitrogen gas at a flow rate of 25 mL/min was used as the environment.

Raman and attenuated total reflection (ATR)-FTIR spectroscopy: Raman spectroscopy was performed on a Horiba HR800 with laser wavelength of 785 nm. The ATR-FTIR spectroscopy was performed on a Nexus 870 FTIR with ATR attachment in order to measure samples with thickness below 100 nm.

The X-ray diffraction (XRD) data is collected with a Rigaku Smartlab diffractometer operated at 45 kV and 200 mA with CuKα1(0.154 nm) radiation. The length-limiting slit for the incident beam is 15mm. 2-dimensional XRD mapping is performed via "Bruker D8 Discover with GADDS" using the same configuration as described in the previous literature (*22*). The Atomic Force Microscope (AFM) images are taken with a Veeco Dimension 3100 AFM. UV-vis-NIR spectra are taken with Varian Cary 5000. X-ray photoelectron spectroscopy (XPS) for the polymers were performed under ultrahigh vacuum below 2×10^{-9} Torr using monochromatic Al Kα radiation at 1486.7 eV in a Surface Science Instruments SSX-100 spectrometer. Work function measurements using XPS were conducted with Thermo Scientific K-Alpha Plus spectrometer under the same conditions.

Out-of-plane electrical conductivity measurements:

We use the architecture similar to the ones reported previously (*30, 40-42*) as shown in fig. S3. 50 nm thick Au is deposited on top of 1μm thick SiO_2 (thermally grown on Si wafers) via physical vapor deposition. PEDOT is deposited on top of the Au layer with oCVD, and rinsed with identical HBr solution as mentioned before. The thickness and the deposition temperature of the PEDOT layer is listed in Table 1 in the main text. In order to reduce the contact resistance, we use liquid metal alloy, Gallium-Indium eutectic (purchased from Sigma Aldrich), as the electrodes and insert copper wires inside the liquid metal droplets. Gallium-Indium eutectic cannot wet on the surface of PEDOT, therefore we use colloidal silver (purchased from TED PELLA) with known area (area determined by camera) as the wetting layer between Ga-In eutectic and PEDOT. By doing this, we also solved the problem of fixing the area of Ga-In liquid electrodes on PEDOT. The out-of-plane resistivity $\rho_\perp$ is calculated from $R_\perp = \rho_\perp L / S$, where $R_\perp$ is the measured resistance with contact resistance (measured separately) deducted, L is the thickness of the thin film and S is the area of top electrode (*30, 41, 42*) . As Ga-In liquid does not wet on PEDOT surface, we use the area of the colloidal silver wetting layer as S. Note here that by using the Ga-In liquid electrodes, the contact resistance can be as low as ~0.4 Ω, which is much lower than the typical contact resistance reported in literature (1-10Ω) (*30*). The low contact resistance allows more accurate measurement of the real vertical resistance of the PEDOT thin films. After calculating resistivity, the out-of-plane electrical conductivity $\sigma_\perp$ is calculated by $\sigma_\perp = 1/\rho_\perp$.

RF Rectifier fabrication:

We start the fabrication of PEDOT-Si radio frequency (RF) rectifier with a 4-inch silicon wafer (n-type Si wafer <100>, Nova Electronic Materials). The silicon wafer is immersed in buffered oxide etch (BOE) (5:1) for about one minute to remove native silicon dioxide from its surface. E-beam lithography (EBL) is used to define the Ohmic metal contact and alignment mark pattern on the silicon wafer with PMMA (*poly(methyl methacrylate)*) as e-beam resist. The mixture solution of methyl isobutyl ketone (MIBK):

isopropanol (IPA) (1:3) is used to develop the EBL exposed pattern. Then 5nm Ti (adhesion layer)/50nm Au is deposited by e-beam evaporation to form Ohmic contact with silicon. After liftoff and cleaning, thin PEDOT film (~20nm) is directly deposited on the Si wafer at 270 ℃ to form Schottky contact by oCVD method. A second EBL process is subsequently carried out to define the Ohmic metal contact (5nmTi/50nm Au) with the PEDOT thin film. The separation between the first and second metal contact pads is 10 μm. Finally, a mesa isolation process is performed to isolate each metal pad using O_2 plasma to etch away nearby PEDOT thin film (etching area starts from the metal pad edge and extends to 5 μm in distance, as indicated by the dash line in Fig. 5b in the main text). The left and right metal contacts in Fig. 5b shows different color contrast, because PEDOT thin film covers on top of the right Ti/Au metal pads.

RF Rectification Measurement:

An RF signal at 13.6 MHz is generated through a function generator (Keysight 33250A) and get coupled to the input of the PEDOT-Si rectifier through a bias tee (Picosecond Pulse Labs). A load resistance R_{load} of 10 kΩ, 55 kΩ and 1MΩ is connected with the rectifier in a series configuration. The rectified output voltage (i.e. voltage dropped across the R_{load}) is measured using an oscilloscope (Keysight DSO6054A, 1MΩ impedance). The oscilloscope is connected with the rectifier circuit through a bias tee as well. In the equivalent circuit diagram shown in Fig. 5c of the main text, the capacitance in the circuit is 0.02 μF, and the inductance is 8 mH.

Work function measurement:

Photoelectron spectroscopy measurements are made to evaluate the work function of the oCVD PEDOT films using focused monochromatic Al *Kα* radiation (photon energy, $h\nu$ = 1486.7 eV) in a Thermo Scientific K-Alpha Plus spectrometer. During the measurements, the samples are biased negatively with respect to earth (V_{bias} = -30 V) in order to accelerate the emitted electrons and hence to detect the onset of emission. The onset kinetic energy ($E_{cut\text{-}off}$), which is the energy of free electrons generated by the photoelectric effect, and the Fermi level (E_F) position are measured, and then the work function (Φ) is determined by the equation below with the photon energy $h\nu$ (1486.7 eV in this study)

$$\Phi = h\nu + E_{cut-off} - E_F \quad \text{(S2)}$$

Before the measurements, gold specimen is used as reference to calibrate the spectrometer and the binding energy scale, which allows accurate determinations of onset energy and Fermi level position. The work function of the gold is measured to be 5.1 eV, which is in a good agreement with the reported value (*43*), which validates reliability of the work function measurements.

Below is an example about the measurement method:

In order to determine the work function of 190℃ “edge-on” PEDOT, XPS Fermi level (E_F) and cut-off energy ($E_{cut\text{-}off}$) measurements were made and the typical plots are shown in fig. S4a and b, respectively. The high-energy cut-off point for the 190℃ edge-on PEDOT is extracted at the contact point of two tangential lines of the plot and the excitation energy is found to be ~1515.73 eV, where the Fermi energy location can be determined. Figure S4b displays the electron cut-off point of the 190℃ edge-on PEDOT.

To determine the energy defined by the cut-off point, a straight line was fitted to the linear regime of the plot which resulted in a baseline intersection point of 34.34 eV. Then the work function of the PEDOT samples is calculated from equation S2.

According to the equation and the values obtained from the E_F and $E_{cut\text{-}off}$ measurements, the work function of the 190℃ edge-on PEDOT is determined to be 5.31 eV and the measurements were repeated for the samples investigated in the present study whose values are very similar to each other regardless of the deposition temperatures (> 190 °C) or crystallization orientation.

Section S2. Additional information about the XRD results and the surface morphology change reflecting the transition of crystallization orientation and crystallinity

The raw XRD results (taken by Rigaku Smartlab) used to generate Fig. 1e in the main text are shown in fig. S5. Figure S5a shows the results of "edge-on" samples, and fig. S5b shows the results of "face-on" samples. The deposition temperature and the film thickness of each sample are included in fig. S5. The peak information in Fig. 1e and fig. S5 is listed in table S1. Note here that, since the Lorentz-polarization (Lp) factor ($Lp(\theta) = \frac{1+\cos^2(2\theta)}{\sin^2\theta\cos\theta}$) is much larger at smaller 2θ when 2θ<90°, the integrated peak intensity (*23*) of the "edge-on" (2θ ~ 6.5°) configuration is much larger than the "face-on" configuration (2θ ~26°), and this phenomenon is regardless of actual crystallinity. Therefore, in order to visualize the peak intensity of both kinds in the same figure, in Fig. 1e in the main text, the "edge-on" peak intensity is converted to equivalent "face-on" peak intensity by considering Lorentz-polarization factor.

Also, since the intensity of "edge-on" peak is much higher than "face-on" peak due to higher Lp factor, the "face-on" peaks in the 222 nm 250 ℃-grown and 172 nm 220℃-grown samples are not obvious in fig. S5a. Figure S5c provides the zoom-in figure of the "face-on" region of the spectra shown in fig. S5a. By converting the "edge-on" peak intensity to equivalent "face-on" peak intensity, the "face-on" peaks in these two samples can be visualized in Fig. 1e in the main text. The coexistence of "face-on" and "edge-on" peaks in the higher temperature-grown thick samples may indicate the reorientation of the crystallites during the oCVD growth process. In addition, in the "edge-on" region (red) of Fig. 1e, it is observed that the "edge-on" peak intensity decreases with deposition temperature increasing, while the "face-on" peak intensity increases as the deposition temperature increases. This phenomena may be related to the preference of high growth temperature for "face-on" configuration, as shown in Fig. 1e and the main text.

We also estimated the crystalline domain size (table S2) using Scherrer equation (*22*, *23*). The estimated crystalline domain size in each regime ("face-on" or "edge-on") does not show a very clear trend in terms of deposition temperature, and the estimated crystalline domain size is in agreement with previous literature (*22*). As we showed in the main text, the crystallinity increases with the deposition temperature increasing in the "face-on" regime. Therefore the enhancement of electrical conductivity is mainly due to the crystallinity enhancement as deposition temperature increases in the "face-on" regime. In addition, the "edge-on" crystallite is larger than the "face-on" crystallite in general, despite the "face-on" samples have higher in-plane conductivity. Therefore other factors, such as the energy barrier between crystallites as we analyzed in the main text, must control the conductivity. Additionally, in fig. S5a, the peak at 2θ~14° for

some samples is the second-order reflection (200) of the same “edge-on” orientation (h00) of the peak at 2θ~6.5˚(100) (*8, 12*).

The transition in crystallization orientation and the change in crystallinity (characterized by the integrated peak-intensity) induce drastic change in surface morphology. Figure S6a and b are the height AFM images for 150℃-grown “edge-on” sample and 300℃ “face-on” sample respectively. The morphology of the latter is in agreement with the previous study of the “edge-on” to “face-on” transition in thin conjugated polymer films(*44*). In addition, the roughness of the samples changes from 2.85 nm to 19 nm as the deposition temperature increases from 150℃ to 300℃ , which may be induced by the enhanced crystallinity and the resulting stacking orientation transition.

Figure S6c and d are the zoom-in phase AFM images for 150℃-grown “edge-on” sample and 300℃ “face-on” sample respectively. The phase AFM images characterize the difference in surface stiffness/softness and adhesion between the tip and surface. Therefore, they are very powerful tools to map the composition difference on the surface. In the “edge-on” sample shown in fig. S6c, there exist big nodular domains with low phase shift (dark, low stiffness) and small needle-like domains with high phase shift (bright, high stiffness) between the nodular dark domains. This interconnecting domains may reflect the amorphous regions and crystallites in the polymeric thin films. In contrast, the morphology of the “face-on” sample shown in fig. S6d is fundamentally different from the one in fig. S6c. In fig. S6d, there are ordered fibrillar domains (bright, high stiffness) with dark domains in between. The intrinsically different morphology may indicate the difference in the arrangement of crystallized domains and crystallinity. These difference eventually will be reflected in the properties of charge carrier transport.

Figure S6e and f show the measurement of film thickness for the 150℃-grown “edge-on” sample and 300℃ “face-on” sample studied in the rest of fig. S6.

Section S3. Thermal stability of oCVD-grown PEDOT thin films

We use TGA in order to study the thermal stability of oCVD-grown PEDOT thin films. As shown in fig. S7, the decomposition temperature of oCVD-grown PEDOT is ~320℃. This result is also in agreement with our observation: with growth temperature higher than 300℃, such as 330℃ and 360℃, no polymeric film was obtained using oCVD technique. Therefore 300℃ is about the highest deposition temperature that we can achieve.

The measured decomposition temperature also agrees very well with reported literature values (*45-47*). Kang *et al.* (*45*) reported a decomposition temperature of 340℃ for PEDOT backbones, Farukh *et al.* (*46*) reported the decomposition temperature of PEDOT backbone as 380℃ . Kiebooms *et al.* (*47*) also reported decomposition temperature above 300℃ for doped PEDOT backbone.

Note here that the counter-ion in oCVD PEDOT thin films is Cl^-/Br^- instead of Polystyrene sulfonate(PSS) (e.g. in PEDOT:PSS). The decomposition temperature of the PSS part starts at 250-260℃ (*45, 48*) in PEDOT:PSS. Therefore, the absence of polymeric counter ion largely enhanced the thermal stability of the oCVD PEDOT thin films, compared to PEDOT:PSS.

Section S4. Raman/FTIR/XPS of oCVD PEDOT thin films

The Raman Spectra are shown in fig. S8. The full spectra for PEDOT samples deposited at different temperatures and with different crystallization orientations are shown in fig. S8a. In fig. S8a, the peaks do not vary with different deposition temperature or different crystallization orientations, indicating a consistent chemical structure for the PEDOT thin films grown with oCVD. In the expanded spectra (fig. S8b), the strong peak at ~1410 cm^{-1} is the characteristic peak of symmetric C_α=C_β stretching (*49-51*). According to Ouyang *et al.* (*51*) and Im *et al.* (*50*), the C_α=C_β stretching peak at relatively lower wavelength of 1410 cm^{-1} is a result of doped quinoid structure (longer conjugation) (*49*), which is also consistent with the high carrier density of ~$2\times10^{21}cm^{-3}$ in this work. The shoulder peak at ~1350 cm^{-1} is attributed to C_β-C_β stretching (*35, 49*). The peak at ~1246 cm^{-1} is corresponding to C_α=C_α, inter-ring stretching (*35*). These peaks are characteristic for PEDOT, and prove the conjugated backbones of the oCVD grown thin films.

The chemical structure of oCVD PEDOT is further confirmed by attenuated total reflection (ATR)-FTIR results (fig. S9). Figure S9a shows the ATR-FTIR results for oCVD PEDOT samples. The deposition temperature and the crystallization orientation are marked in the figure. Figure S9b shows the FTIR spectrum for 300℃-grown "face-on" PEDOT sample only. The FTIR spectra of oCVD PEDOT shows similar primary features as PEDOT:PSS films (*49, 50*) and as previously reported oCVD PEDOT samples (*49*). The characteristic peaks for PEDOT are: C=C stretching mode in thiophene rings at 1520 cm^{-1} (*49*), C-C stretching mode in thiophene rings at 1340 cm^{-1} (*49*), C-O-C bond stretching modes of the ethylenedioxy group at 1184 cm^{-1} and 1132 cm^{-1} (*49*), C-O bond stretching in the ethylenedioxy group at 1049 cm^{-1} (*49*), C-S bond vibrations at 971 cm^{-1}, 830 cm^{-1}, and 692 cm^{-1} (*49*), as well as the deformation mode of ethylenedioxy rings at 920 cm^{-1} (*49*).

Figure S10 shows the XPS results for oCVD PEDOT thin films. Figure S10a shows the survey scan for 190℃ "edge-on", 190℃ "face-on" and 300℃ "face-on" samples. The presence of Fe is only observed with trace amount in 190℃ "edge-on" samples. According to Lee *et al.* (*5*) and Howden *et al.* (*35*), oCVD PEDOT samples before HBr treatment have a sharp and prominent peak for Fe2p at ~710 eV(*5*). After HBr treatment, the Fe containing compounds can be removed (*5, 35*).

Figure S10 b-d show the C1s peak for oCVD PEDOT samples. Peak analysis is conducted as shown in the figure: C-C/C-H bond is attributed to 284.6 eV (*52*), C-S bond is corresponding to 285.3 eV (*52*). The conjugated C=C-O bond contributes the peak at ~286.3 eV (*53*), and the C-O-C bond in the ethylenedioxy ring is ~287 eV (*53*). π-π* shake-up transition contributes the peak at~290 eV (*52, 53*). The presence of C=C-O peak in the XPS analysis again confirms the conjugated backbone structure of the conducting polymer thin films we obtained.

Section S5. The influence of film thickness on electrical conductivity and batch reproducibility

Film thickness, as shown in Fig. 1e, is a key parameter to determine the crystallization orientation and therefore has impact on the electrical conductivity. This section provides a detailed discussion about how the film thickness influences the conductivity. Figure S11a shows the room-temperature electrical conductivity change with the film thickness in the deposition temperature range from 150℃ to 300℃.

From fig. S11a, it is observed that with the thickness greater than 100 nm, the conductivity does not vary with film thickness and is only a function of deposition temperature and post-deposition treatment (w/ or w/o HBr treatment, as described in section S1). Here, with film thickness greater than 100 nm, the PEDOT films exhibit the "edge-on" configuration (Fig. 1 in the main text). However, when the film thickness is below 50 nm, PEDOT thin films demonstrate much higher electrical conductivity compared to the thick films (>100 nm) deposited and treated with the same condition. This is due to the confinement and crystallite orientation transition (from "edge-on" to "face-on") discussed in the main text. In order to make consistent comparison, the film thickness of the "face-on" samples deposited at 250℃ - 300℃ are all kept at ~ 10 nm in Fig. 2a. In addition, the error bars in Fig. 2a denote the 95% confidence interval of 7 measurements among one typical batch. As a complement, fig. S11b shows the number-average of the measured electrical conductivity on multiple samples grown at the same experimental conditions but from different batches. The average value and deviation from batch to batch is about the same as the samples deposited from one batch.

Section S6. Summarizing the room temperature electrical properties of the oCVD PEDOT samples

For the convenience of readers, table S3 summarizes the results of the PEDOT samples we discussed in the main text.

Section S7. The effect of HBr rinsing on work function and optical properties

All the samples studied in the main text and in the rest of Supplementary Materials are treated with HBr solution after deposition in order to enhance their electrical conductivity. This section and section S8 provide a detailed discussion about the effect of HBr treatment. Section S7 and section S8 are relatively independent to other sections in the Supplementary Materials and the main text, since the rest of the paper only concerns HBr treated cases.

The effect of HBr treatment is mainly to enhance the effective carrier density, and hence to enhance the electrical conductivity. Figure S12a shows the work function (measured by XPS) of PEDOT deposited at different temperatures. The work function of samples is ~5.5 eV and 5.3 eV for samples before and after HBr treatment respectively. Systematically, HBr treatment decreases the work function, and the work function of PEDOT decreases with increasing doping level (*29*). Therefore, the decrease of the work function by HBr treatment indicates an increased doping level, or carrier density. This may due to the removal of non-ionized impurities and counter-ion exchange by HBr rinsing (*35*).

The effect of HBr rinsing is further studied with an optical approach using ultraviolet-visible-near infrared (UV-vis-NIR) spectra. Figure S12b shows the thickness normalized UV-vis-NIR spectra of two "edge-on" samples deposited at 220℃ and 250℃. The HBr treatment enhances the (bi)polaron absorption (*18*) in the near IR region beyond 700 nm, which indicates an enhanced charge carrier ((bi)polaron) concentration.

As shown in fig. S12c, for the "face-on" samples deposited at 270℃ and 300℃, HBr treatment drastically changed the UV-vis-NIR absorption, especially in the near IR region and the region below 400 nm. For the "face-on" samples deposited at 270℃ and 300℃, the as-deposited sample before HBr treatment shows a large absorption peak at ~303 nm. This is due to some impurity structure formed at high temperatures. The impurity also leads to a yellowish color for the thin film. After HBr rinsing, the

impurities are removed, and the peak at ~303 nm is bleached. The main absorption of polarons (or bipolarons) at the wavelength ~770 nm and beyond begin to dominate (*18*). The high absorption in the near IR region of the HBr rinsed samples suggests a high doping level induced by removing undoped impurities for the ultrathin films. Figure S12d shows that the transmittance of the "face-on" films is much improved by HBr treatment in the visible range, mainly because of the removal of non-ionized impurities, such as Fe containing non-conductive hydration complex or oxides (*5, 35*). The plasma frequency can be written as $\omega_p^2 = \frac{ne^2}{m^* \varepsilon_0}$ in SI units (*12, 18*). Using the results of the theoretical analysis, with n~2×10^{21} cm^{-3} (300℃ "face-on" sample), we can calculate that $\hbar\omega_p = 1.67eV$ ($m^* \sim m_e$), which corresponds to 742 nm in the infrared region. The infrared plasma frequency ensures the main absorption is in the IR region (*12, 18*). The tail absorption in the wavelength shorter than 742 nm may due to the interband π-π∗ transitions between the partially filled conduction band and the lowest energy unoccupied band (*18*). Figure S12e shows the thickness normalized UV-vis-NIR absorption of all the HBr treated oCVD PEDOT thin films.

Section S8. The effect of HBr rinsing on crystallization and surface morphology

Figure S13a, b and c shows the XRD results for various PEDOT samples before and after HBr treatment. Figure S13a shows the XRD results for "edge-on" PEDOT samples grown at 220℃ and 250℃. In general, the peak intensity is decreased after HBr treatment. This may be an effect due to the disturbance of the lattice by increased effective carrier density. Figure S13b shows the XRD results of 270℃-grown "face-on" samples. The pattern is not affected by HBr treatment significantly. However, since at high deposition temperature the film growth rate is much reduced, the presence of non-ionized impurities, such as Fe containing non-conductive hydration complexes or oxides (*5, 35*), are more common. As shown in fig. S13c, in XRD pattern of the ultrathin films deposited at 300℃ before HBr treatment, there is a peak (2θ~12˚) corresponding to the impurity. Comparing with the HBr treated XRD pattern shown in fig. S13c, we can observe that HBr treatment removes the impurity. The same phenomena is shown in the 2D XRD map in fig. S13d as well.

Figure S14 shows the height AFM images for various PEDOT samples before and after HBr treatment. The surface morphology is not changed significantly by HBr treatment, while the deposition temperature play an important role in determining the surface morphology.

Section S9. The mechanism of crystallization-orientation transition

As stated in the main text, the crystallization-orientation transition from "edge-on" to "face-on" is related to *(1) low film thickness* and *(2) high deposition temperature*. This part will provide more discussion about the mechanism of such transition.

We hypothesize that the crystallization process of oCVD PEDOT happens during both the film-growth process as well as the cooling process after the oCVD growth under vacuum. The just-formed polymer chains may not have a certain preferred crystallization form. During crystallization process, the preferred crystallization-orientation forms, and for thick films, it is "edge-on". However, when the film thickness is so small (i.e. ~10 nm in main text) that it is comparable to the stacking length along the stacking direction of the crystallite (~6.8 nm for "edge-on" as discussed in main text), the effect of confinement may make it

more thermodynamically preferred to adopt a “face-on” orientation which is smaller (~3.2 nm) and might provide energy minimization. This may explain the effect that *low film thickness* is preferred for “face-on” crystallite formation. The crystallization process may happen during the growth process as well as the cooling process. During the crystallite-forming process, the high deposition temperature may lead to higher chain mobility for the polymer chains in the growing films, and thus is beneficial for any reorientation process in order to achieve energy minimization. In addition, high deposition temperature leads to longer cooling time, which is also beneficial for achieving the thermodynamically preferred configuration. This may explain the effect that *high deposition temperature* is preferred for “face-on” crystallite formation.

The crystallization process in oCVD PEDOT films is also in analogy to the crystallization orientation transition during the crystallization of polymers from melts in a confined ultrathin layer. From such crystallization study, researchers have observed that thicker films tend to induce “edge-on” lamellae, while in thinner films the “flat-on” orientation is preferred (*54*). The potential reason is that, in the thin films, the interfacial properties dominates. The chain mobility on the free interface will be higher than the chain mobility on the bottom interface between polymers and the substrate. This chain mobility difference will result in a difference in the crystallization temperature T_c, which will further induce a difference in the crystallization rate on different interfaces at the same temperature. Therefore, at a certain system temperature, if the crystallization rate on the bottom interface is higher, then the nucleation will start from bottom, and “flat-on” orientation is preferred in the ultrathin films. On the other hand, in the thick films, the interfacial properties does not have an equally big influence, and the “edge-on” configuration is preferred.

Section S10. The discussion about Seebeck coefficient measurement

In addition to the procedures described in section S1, in this section further discussion about the Seebeck coefficient measurements is provided. Figure S2a shows the set-up for the Seebeck coefficient (S) measurement. The room temperature Seebeck coefficients for all the samples lie in a very narrow range (10-13 μV/K), corresponding to $E_F - E_t$ of ~0.6±0.07 eV (Fig. 3a and fig. S15a). We treat the variation in the Seebeck coefficient as within the experimental error and use $E_F - E_t$ =0.6 eV for all the samples in the analysis. This low Seebeck coefficient indicates a high charge carrier density in the oCVD PEDOT films. We use this information to further understand the change of σ_{E0} and carrier mobility. As discussed in the main text, the carrier density calculated using Seebeck coefficient and electrical conductivity is ~2.12×10^{21} cm^{-3}. The calculated carrier density is also validated by Hall effect measurement result ($2.73(\pm0.9)\times10^{21}$ cm^{-3}). The carrier density of the oCVD PEDOT thin films lies in the range of a typical metallic conjugated polymer (n~$2\text{-}5\times10^{21}$ cm^{-3}) (*5*, *18*).

In addition, since

$$n = \frac{1}{2\pi^2}\left(\frac{2m^* k_B T}{\hbar^2}\right)^{\frac{3}{2}} F_{1/2}(\eta) \tag{S3}$$

where $\eta = \frac{E_F - E_t}{k_B T}$, the charge carrier density *n* at a certain temperature is actually solely related to Seebeck coefficient. Or Seebeck coefficient is solely determined by the charge carrier density at a given temperature in this model.

Section S11. Sensitivity analysis of the Seebeck coefficient measurement

Since the carrier mobility calculation is related to the Seebeck coefficient, sensitivity analysis considering the measurement error of Seebeck coefficient is necessary. Figure S15b shows the sensitivity analysis of the impact of Seebeck coefficient measurement error to the carrier mobility calculation. From the Kang-Snyder model, the Seebeck coefficient was determined by the energy difference between Fermi level E_F and the transport edge E_t (or the charge carrier density, as stated in sections S1 and S10). We used the measured Seebeck coefficient to infer this energy difference, and further use this difference to calculate the charge carrier density and the carrier mobility of the PEDOT films. Since the Seebeck coefficient does not change significantly among different samples and are all within the measurement error (section S10), we use the average value of the calculated $E_F - E_t$ =0.6 eV for the following calculations. The assumption of same $E_F - E_t$ for all the HBr treated samples is supported by XPS work function measurement results (Fig. 3a in the main text) with similar work function (5.33(±0.04) eV) for all the HBr treated samples. Therefore the Fermi level, E_F , is similar among all the samples. If the transport edge E_t is similar among the samples, then $E_F - E_t$ should be the similar for all the samples. Here we discuss the effect of the small variation of Seebeck coefficient among all the samples on the calculated results of charge carrier concentration *n* and carrier mobility μ .

The calculated $E_F - E_t$ varies in the range of 0.55 to 0.7 eV, from the measured Seebeck coefficient. With, $E_F - E_t$ = 0.55 eV, the final charge carrier density at room temperature is 2.67×10^{21} cm^{-3}, while with $E_F - E_t$ =0.7 eV, the final charge carrier density at room temperature is 1.86×10^{21} cm^{-3}. Compared to the calculated *n* of 2.12×10^{21} cm^{-3} in the main text, the error is within 30%.

With the equation $\sigma = nq\mu$ and the sensitivity analysis on charge carrier density, we can estimate the influence of Seebeck coefficient measurement error on the carrier mobility. The highest room temperature mobility originated from the "face-on" sample deposited at 300°C with σ=6259 S/cm. If n=1.86×10^{21} cm^{-3}, μ=21 $cm^2V^{-1}s^{-1}$; if n=2.67×10^{21} cm^{-3}, μ=14.9 $cm^2V^{-1}s^{-1}$. Figure S15b plots the calculated mobility of "face-on" samples with upper and lower bounds originated from the Seebeck coefficient measurement. The Hall effect measured mobility for the "face-on" sample deposited at 300°C is 26.6±9 $cm^2V^{-1}s^{-1}$. The upper and lower boundaries of the mobility calculation error are both in the range of mobility measurement error. The main conclusion is robust to this experimental error. The main reason for the extraordinarily excellent electrical conductivity of the oCVD PEDOT here is the high carrier mobility maintained at high carrier density.

Section S12. The energy barrier W_γ

Using the cryogenic result and the assumption that $E_F - E_t$ does not change with temperature, we get the temperature-dependent σ_{E0} and carrier mobility in fig. S16a and Fig. 3d respectively. The samples analyzed in these two figures are "face-on" samples with deposition temperatures of 300℃ and 190℃, and the "edge-on" sample with deposition temperature of 190℃. With higher deposition temperature, the carrier mobility is significantly enhanced in Fig. 3d.

As stated in the main text, in the inhomogeneous disorder model, $\sigma_{E0}(T)$ is positively correlated to $\exp[-(\frac{W_\gamma}{k_B T})^\gamma]$ where W_γ is the energy barrier for inter-crystallite carrier transport, and γ is a parameter which is usually ½.(*9*) Here we use, $\sigma_{E0}(T) = \sigma_{E00} + \alpha \exp[-(\frac{W_\gamma}{k_B T})^\gamma]$, where σ_{E00} is the σ_{E0} when T= 0K and α is the proportional factor of the exponential term (*18*). This equation is a modification of the Kang-Snyder model, in order to reconcile the contradiction between non-zero conductivity approaching 0K for some conducting polymers (*9, 18*) and the zero conductivity at 0K doomed by the original K-S model. According to equation (2) in the main text, the parameter σ_{E00} should be temperature-dependent if the model will lead to a finite conductivity at 0K. However, the carrier transport mechanism in the low temperature region near 0K is very unclear and hard to model with a clear mathematical representation. For simplicity, at the relatively high temperature regime (>40K), we assume σ_{E00} is a positive constant. This assumption makes sense since the parameter σ_{E00} is related to the intrinsic carrier conduction regardless of the temperature-activated hopping.

The parameters fitted from this model is shown in table S4, and the fitted σ_{E0} is plotted in fig. S16b. We noticed that the parameter σ_{E00} of the 190℃ "edge-on" sample is much higher than the "face-on" sample deposited at the same temperature. This is in agreement with the finding of Sirringhaus *et al.* showing that, when the intra-crystallite transport dominates, the "edge-on" stacking has superior in-plane conduction due to the two-dimensional carrier transport enabled by the inter-chain carrier transport due to π-π stacking in the in-plane direction (*10*). The parameter σ_{E00} is separated from the temperature-activated inter-crystallite hopping, and represents only the intrinsic carrier transport due to the crystallization. Furthermore, the σ_{E00} increases with increasing deposition temperature in the "face-on" regime, which is related to the increased crystallinity by elevated deposition temperature.

"Edge-on" stacking's advantage in the intra-crystallite carrier transport is largely overtaken by the disadvantage in the inter-crystallite energy barrierW_γ. From table S4, the energy barrier, W_γ, of the 190℃ "edge-on" sample is 175.4 meV, in the same range (~100 meV) as reported by Sirringhaus *et al.* for regioregular poly(3-hexylthiophene) (*10*). Since W_γ denotes the effect of the disordered region between the crystallized domains, if the W_γ is about the same order-of-magnitude, the dominating factor would be only the intra-crystallite transport, where "edge-on" has advantage. However, as we observed in the results (table S4), the "face-on" samples manifest much smaller energy barriers W_γ compared to

"edge-on" samples, which determines much higher carrier mobility and higher electrical conductivity. In addition, for "face-on" samples, the energy barrier W_γ decreases as the deposition temperature increases due to shorter inter-crystallite distance induced by increased crystallinity.

The small energy barrier indicates an intrinsically different physical picture of inter-crystallite connection in the "face-on" regime. As depicted in Fig. 1a, the connection between crystallites in the pure "face-on" samples (which are only achieved at very thin films (~10 nm) as shown in Fig. 1e in the main text) is largely confined in a thin layer. The connecting polymer chains between two face-on crystallites through a confined space (~3 times of the stacking length, calculated with the crystallite size in the main text) is much likely to be "rod-like" (*28*) and ordered since the out-of-plane dimension of the thin films may be smaller than the dimension of random coil, due to the long polymer-length shared by multiple crystallites and the inherent rigidity of the chains (*32, 55*). The AFM images (fig. S6 and fig. S14) also shows a planar surface in the 300℃ "face-on" samples. As a contrast, the possibility of the formation of "coil-like"(*28*) highly disordered inter-crystallite polymer chains, is much higher in the thick "edge-on" films (248 nm grown at 190℃) due to additional dimension of space that allows the formation of random coil. This will result in a much higher inter-crystallite energy barrier.

Another reason can be the additional conduction path in the out-of-plane direction provided by the π-π stacking in the "face-on" configuration. As Rivnay et al. pointed out, the "face-on" crystallites provide additional conduction path through the out-of- plane direction, due to π-π stacking (*55*). When the conduction through the top few nanometers is important, this additional conduction helps circumvent the defects of the amorphous inter-crystallite region in the in-plane direction, and decreases the inter-crystallite energy barrier. In addition, in the "edge-on" films, any shift, tilt, or rotation of the crystallite will hinder the π-π overlap between two adjacent crystallites, therefore induce huge energy barrier for the inter-crystallite carrier transport(*32*).

The parameter α in table S4 is the proportional factor for the thermal-activated term. It may be related to the thickness of the film, which is proportional to the number of phonon-assisted electron hopping attempts per unit time(*18*). The fitted results of α shown in table S4 are in the same trend with the real sample thickness: 300℃ face-on is 10 nm; 190℃ face-on is 36 nm; 190℃ edge-on is 248 nm.

Section S13. The wafer-scale fabrication of RF rectifier arrays and their performance at other frequencies

The fabrication method of the polymer based RF rectifier arrays is discussed in section S1. Here fig. S17a demonstrates the wafer scale fabrication of RF rectifiers. In the main text, we demonstrate that the rectifier can work at the standard radio frequency of 13.56 MHz. Actually they can work at even larger frequencies. Figure S17b demonstrates the rectification ability at 50 MHz as an example.

Tables:

Table S1. The XRD peak intensity for oCVD PEDOT samples in Fig. 1E.

Deposition Temperature (℃)	Thickness (nm)	Face-on Integrated Intensity (a.u.)	Edge-on raw Integrated Intensity (a.u.)	Edge-on Lp Converted Integrated Intensity* (a.u.)
300	10	173.5	0.0	0.0
270	14	68.8	0.0	0.0
250	11	55.2	0.0	0.0
220	31	27.3	0.0	0.0
190	36	25.2	0.0	0.0
250	222	39.8	715.1	42.3
220	172	13.4	960.5	56.9
190	248	0.0	1782.2	105.5
150	34	0.0	2186.0	129.4

* Convert “edge-on” intensity into equivalent “face-on” intensity by raw “edge-on” intensity × Lp(face-on)/Lp(edge-on)

Table S2. Crystalline domain size estimated from Scherrer equation.

Deposition Temperature (°C)	Crystallization Orientation	FWHM (2θ)	Crystalline Domain Size (nm)
300	face-on	2.6	3.19
270	face-on	2.7	2.99
250	face-on	2.6	3.15
220	face-on	2.3	3.59
190	face-on	2.7	3.02
250	edge-on	1.2	6.79
220	edge-on	1.3	6.52
190	edge-on	1.1	7.41
150	edge-on	1.5	5.35

Table S3. Summary of the growth conditions and the resulting PEDOT thin-film properties for the HBr-rinsed thin films.

Deposition Temperature (℃)	Deposition Time (min)	Average Film Thickness (nm)	Crystallization Orientation	Average In-plane Electrical Conductivity (S/cm)	Average Seebeck Coefficient (μV/K)	Carrier Mobility ($cm^2V^{-1}s^{-1}$)	Average Work Function (eV)
300	120	10	face-on	6258.75	11.26	18.45	5.28
270	90	14	face-on	4730.99	13.29	13.94	5.37
250	30	11	face-on	3511.88	10.63	10.35	
220	30	31	face-on	1966.10	11.91	5.794	
190	20	36	face-on	954.67	9.999	2.814	
250	120	222	edge-on	665.15	12.80	1.960	5.37
220	60	172	edge-on	517.30	11.00	1.525	
190	90	248	edge-on	473.35	10.49	1.395	5.31
150	30	34	edge-on	371.60	11.40	1.095	

Table S4. The fitting results for the parameters in σE0(T).

fitted parameters / sample name	σ_{E00} (S/cm)	W_γ (meV)	α (S/cm)
300℃ face-on	0.0341	0.2	2.7542
190℃ face-on	0.0024	0.6	5.8575
190℃ edge-on	1.8532	175.4	217.14

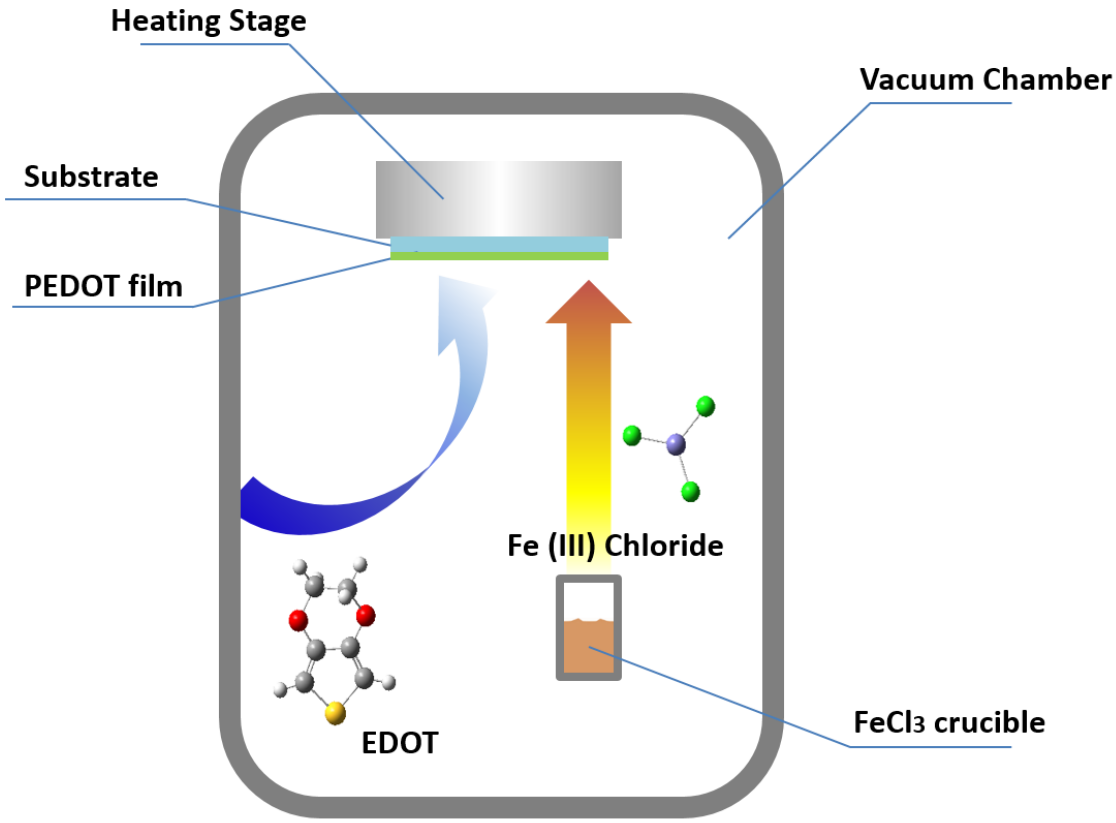

Fig. S1. The schematic of the oCVD process. The oxidant $FeCl_3$ and the monomer EDOT are simultaneously introduced into a vacuum chamber. The deposition takes place on the substrate placed on a heating stage, where the temperature is adjusted.

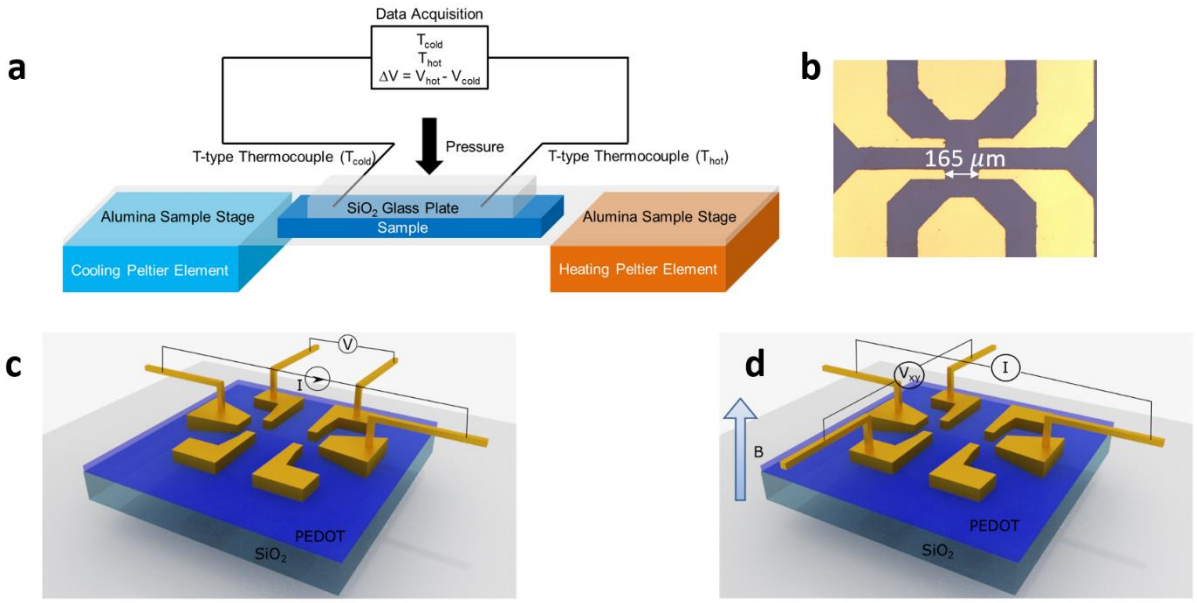

Fig. S2. The thermoelectric and electrical measurements. (**a**). The schematic of Seebeck coefficient measurement installation. (**b**). optical microscope image of the van der pauw device. (**c**). The schematic of the device used in cryogenic conductivity measurement for the temperature-dependent conductivity curve. A van der Pauw type of device is made with gold electrodes and PEDOT film grown on 1μm thick SiO_2 wafer. The conductance is measured with a typical four point method as shown in the figure. (**d**). The schematic of the device used for Hall effect measurement. Here the magnetic field used is 2800 G and the current is 100 mA.

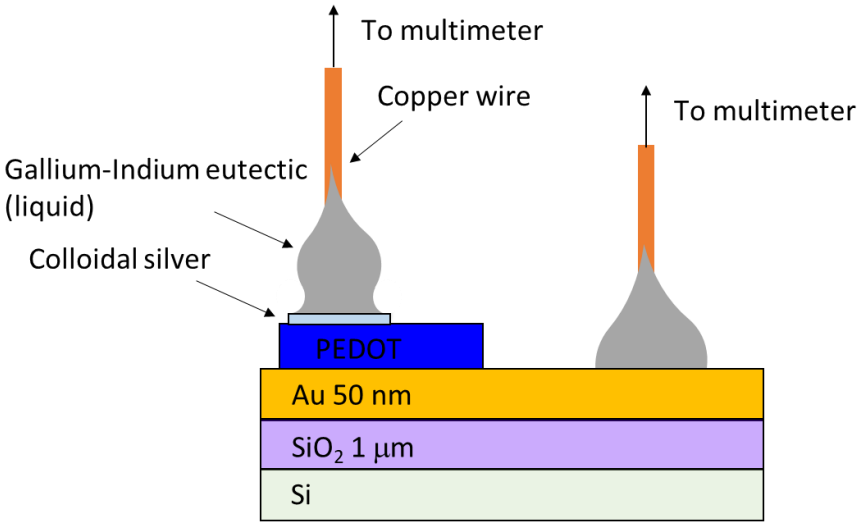

Fig. S3. Schematic representation of out-of-plane conductivity measurement. Liquid metal alloy, Ga-In eutectic, is used as liquid electrodes in order to reduce contact resistance. Colloidal silver is used as wetting layer for the Ga-In eutectic electrodes on PEDOT in order to enhance wetting.

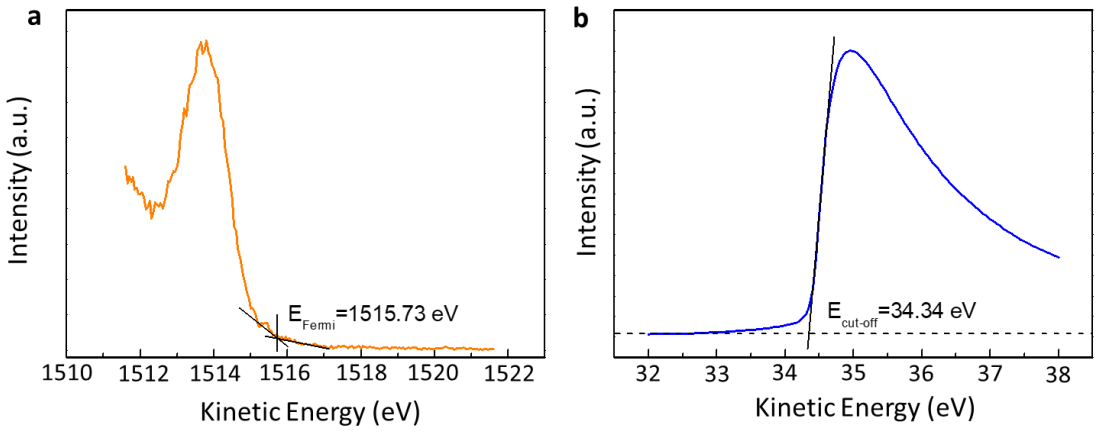

Fig. S4. The work function of PEDOT samples is determined using XPS. (**a**). Fermi level (E_F) and (**b**). cut-off energy ($E_{cut\text{-}off}$) measurements: E_F of HBr rinsed 190℃ "edge-on" sample is found to be ~1515.73 eV and $E_{cut\text{-}off}$ is extrapolated to be ~34.34 eV, through which the work function is determined to be 5.31 eV.

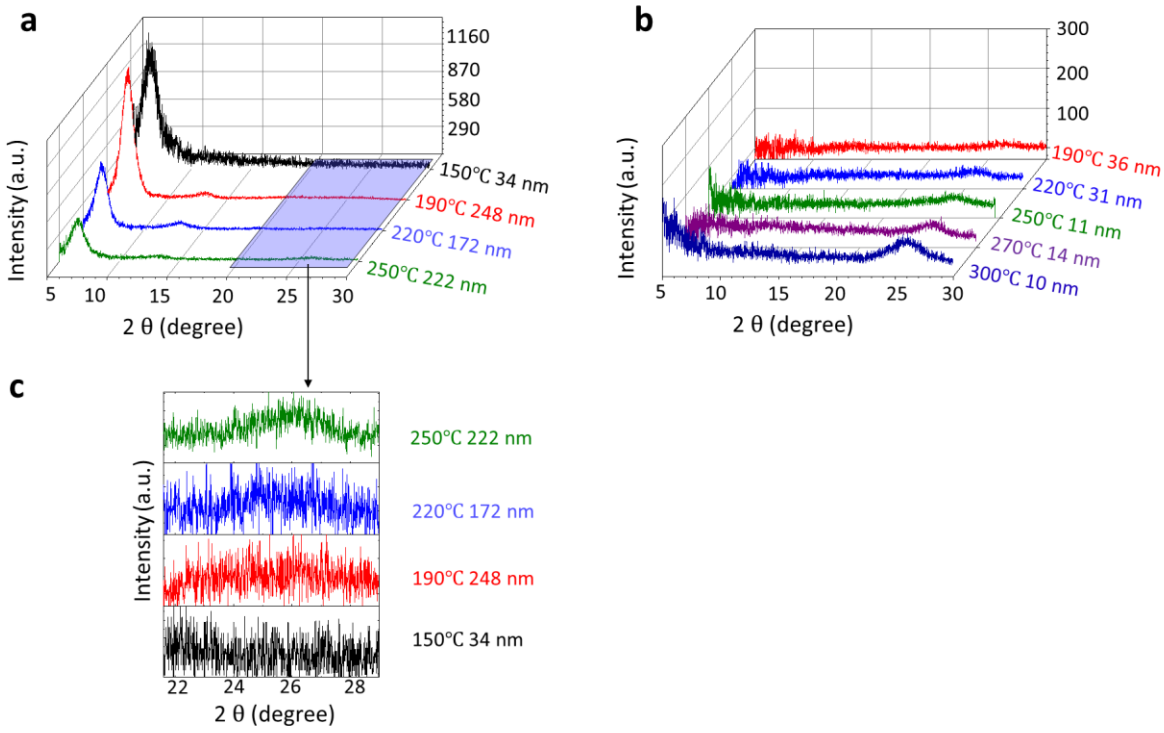

Fig. S5. The room temperature XRD patterns of oCVD PEDOT thin films rinsed with HBr. (**a**). The XRD results of "edge-on" samples. (**b**). The XRD results of "face-on" samples. The deposition temperature and the film thickness are included in the figures. (**c**). zoom-in figure of the 2θ~22-29˚region in a., showing the "face-on" peaks for 250 and 220℃ -grown "edge-on" samples.

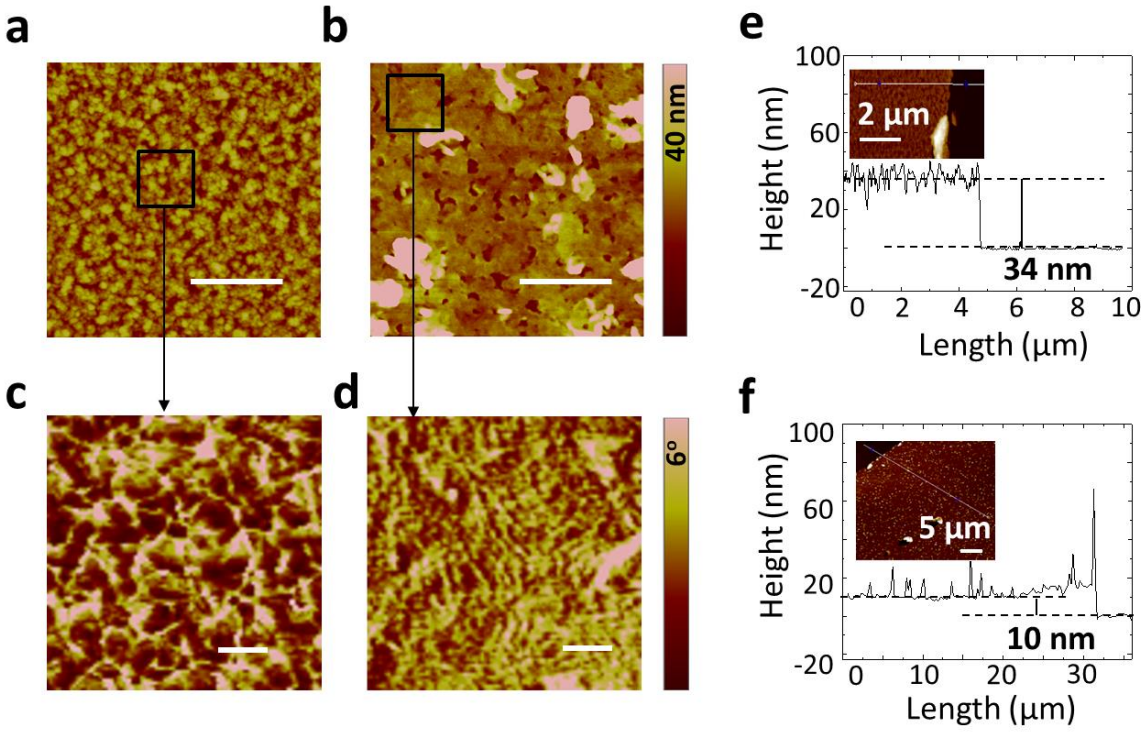

Fig. S6. The surface morphology of PEDOT thin films deposited at different temperatures. (**a**). the height AFM image of PEDOT thin film deposited at 150°C. This sample has "edge-on" crystallization configuration. The scale bar is 1 µm. (**b**). the height AFM image of PEDOT thin film deposited at 300°C. This sample has "face-on" crystallization configuration. The scale bar is 1 µm. (**c**). the zoom-in phase image of 150°C-grown PEDOT thin film. The scale bar is 100 nm. (**d**). the zoom-in phase image of 300°C-grown PEDOT thin film. The scale bar is 100 nm. Note the bright fibrillar domains. (**e**). measuring the thickness of 150°C-grown PEDOT thin film in a. and c. (**f**). measuring the thickness of 300°C-grown PEDOT thin film in b. and d.

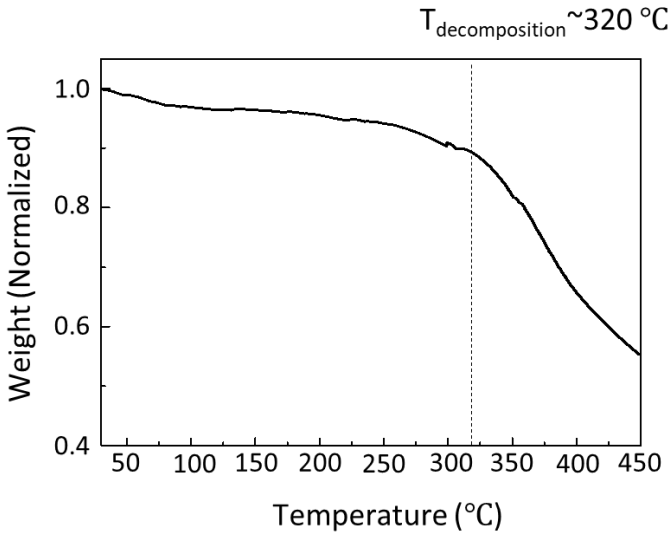

Fig. S7. The thermogravimetric analysis result. Showing the thermally decomposition temperature of the PEDOT thin films is ~320°C, which is above the deposition temperature.

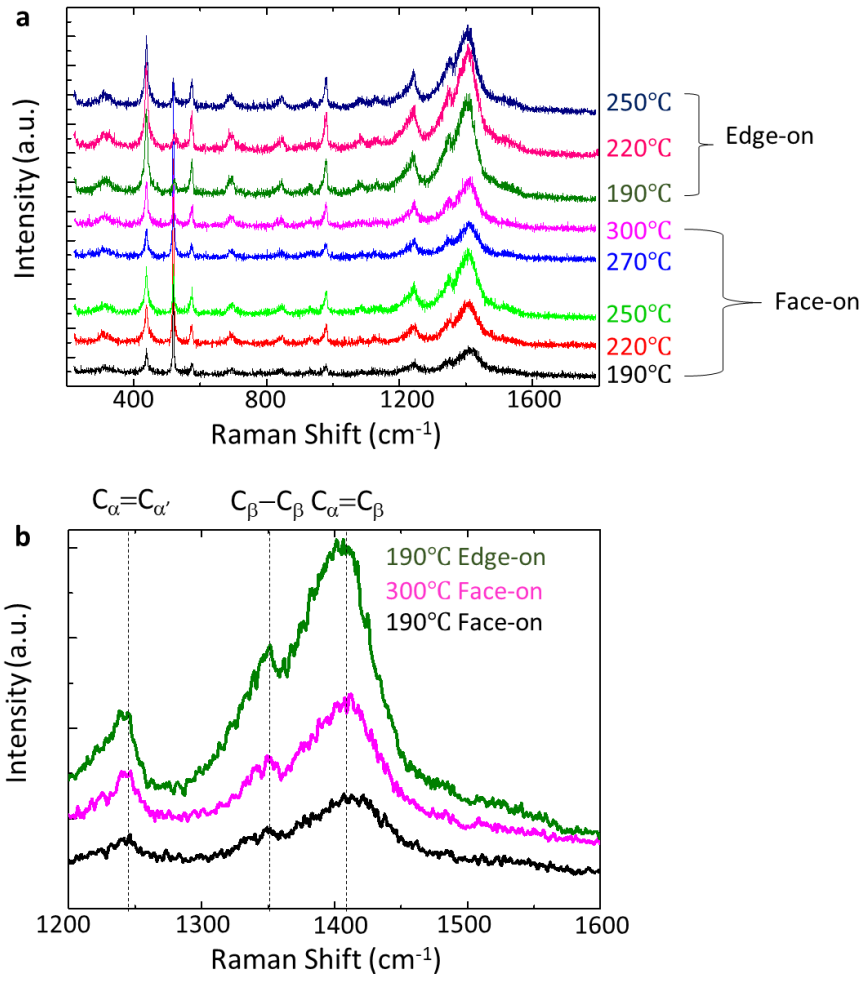

Fig. S8. Room temperature Raman spectra of oCVD PEDOT samples. (**a**). the full spectra (200-1800 cm^{-1}) of oCVD PEDOT samples with different deposition temperature and different crystallization orientation. The deposition temperature and crystallization orientation are marked in the figure. (**b**). the zoom-in spectra expanded around the 1410 cm^{-1} peak. This peak is corresponding to $C_\alpha=C_\beta$ stretching in doped quinoid structure of PEDOT.

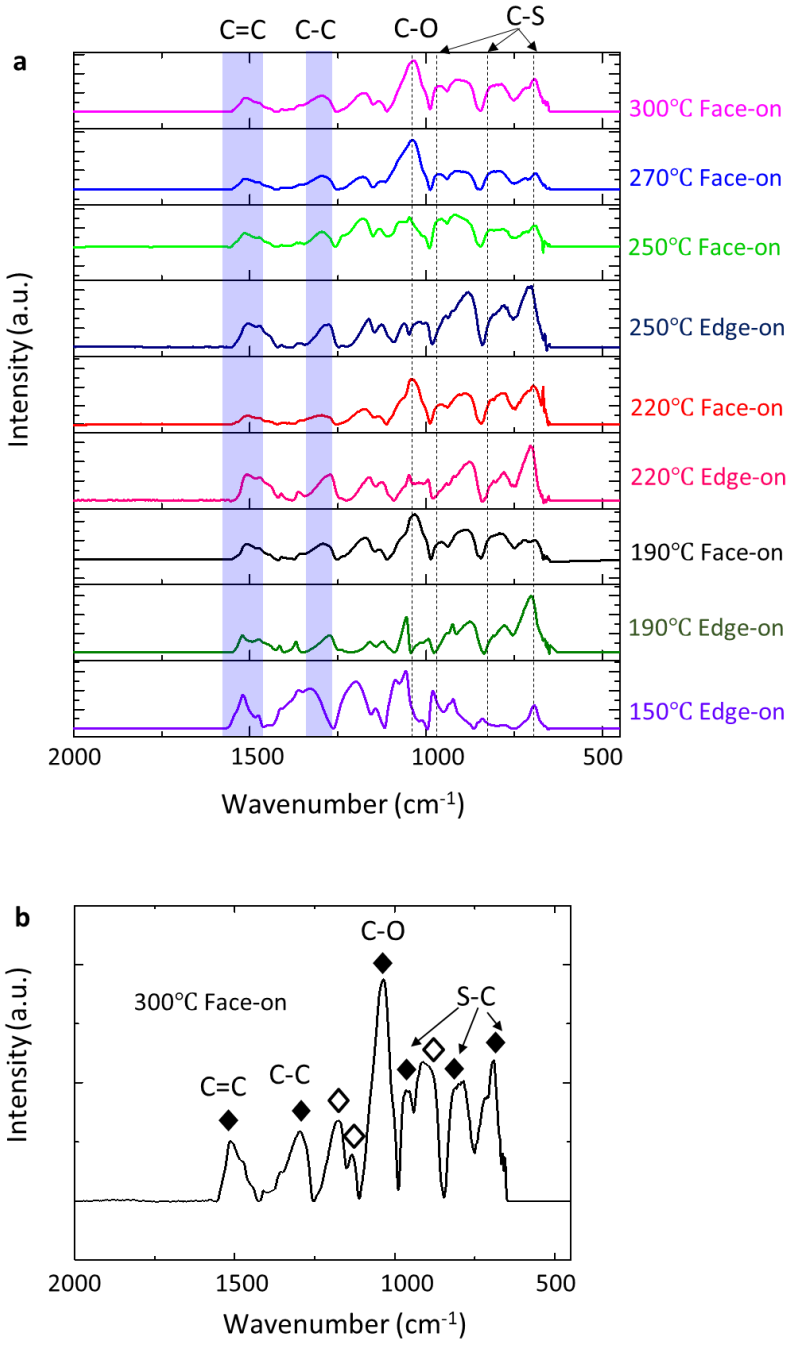

Fig. S9. Room temperature ATR-FTIR results. (**a**). ATR-FTIR results of oCVD PEDOT samples deposited at different temperatures and with different crystallization orientation. The deposition temperature and crystallization orientation are marked in the figure. (**b**). The FTIR spectrum of 300°C-grown "face-on" PEDOT sample. The unlabeled peaks (◇) result from the ethylenedioxy ring.

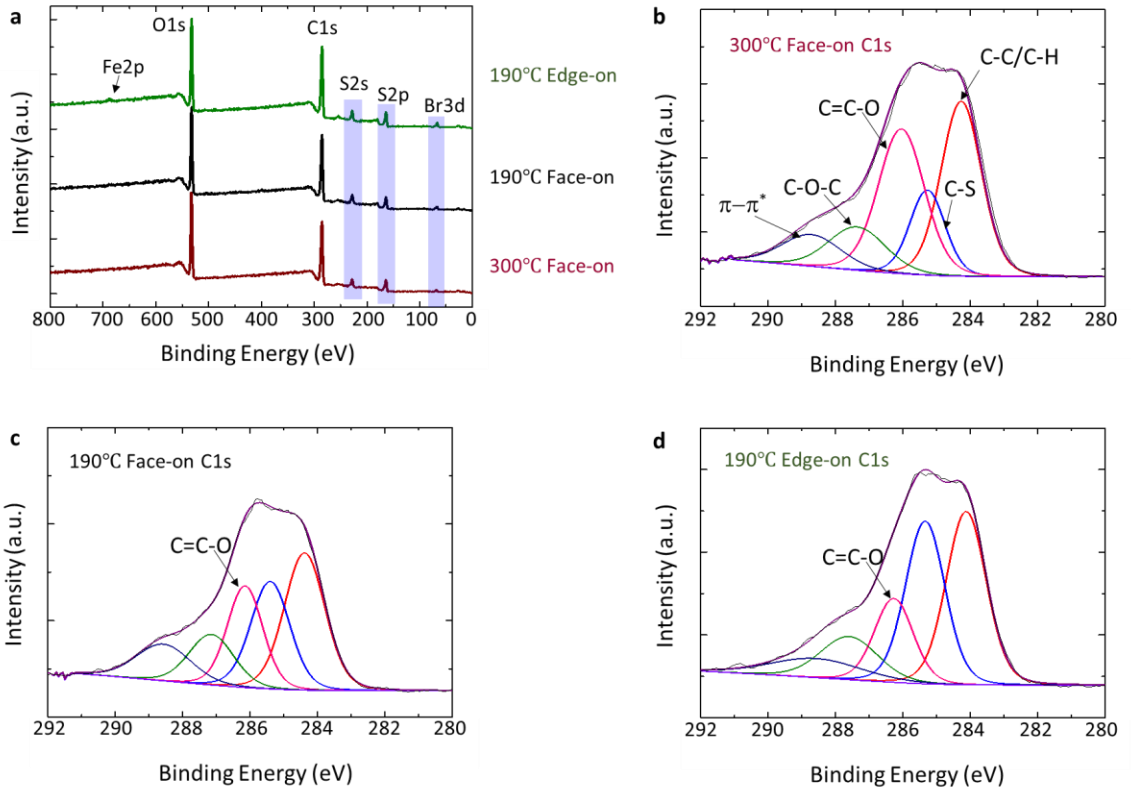

Fig. S10. XPS for oCVD PEDOT. (**a**). survey scan for oCVD PEDOT samples. The deposition temperature and the crystallization orientation are shown in the figure. (**b-d**). the C1s high resolution spectra for 300℃ "face-on" PEDOT thin film, 190℃ "face-on" PEDOT thin film and 190℃ "edge-on" PEDOT thin film respectively.

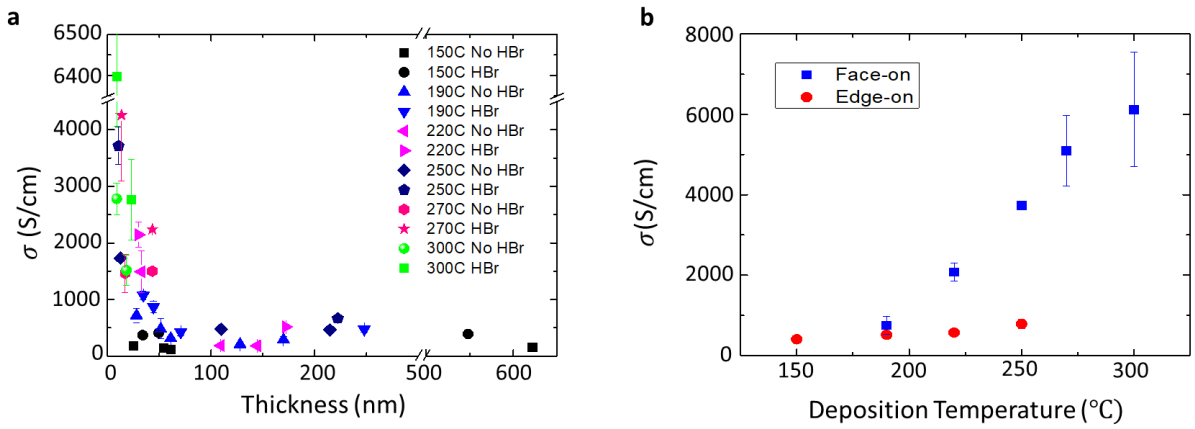

Fig. S11. Supplementary data of the electrical conductivity (σ) measured at room temperature. (**a**). The effect of film thickness to the electrical conductivity. Compared to the thick samples (>100 nm), the ultrathin PEDOT films (<50 nm) deposited at the same temperature and treated with same post-deposition treatment (with or without HBr) exhibit much higher electrical conductivity. In order to rule out the influence of thickness, the "face-on" samples deposited at 250-300 ℃ are kept at ~ 10 nm carefully in Figure 2a in the main text. (**b**). The electrical conductivity of the "face-on" and "edge-on" samples deposited at different temperatures. The error bar here is from measurements on three samples from different batches. The point of 300℃ "face-on" sample is 6122±1424 S/cm, which is about the same as the result in Figure 2a.

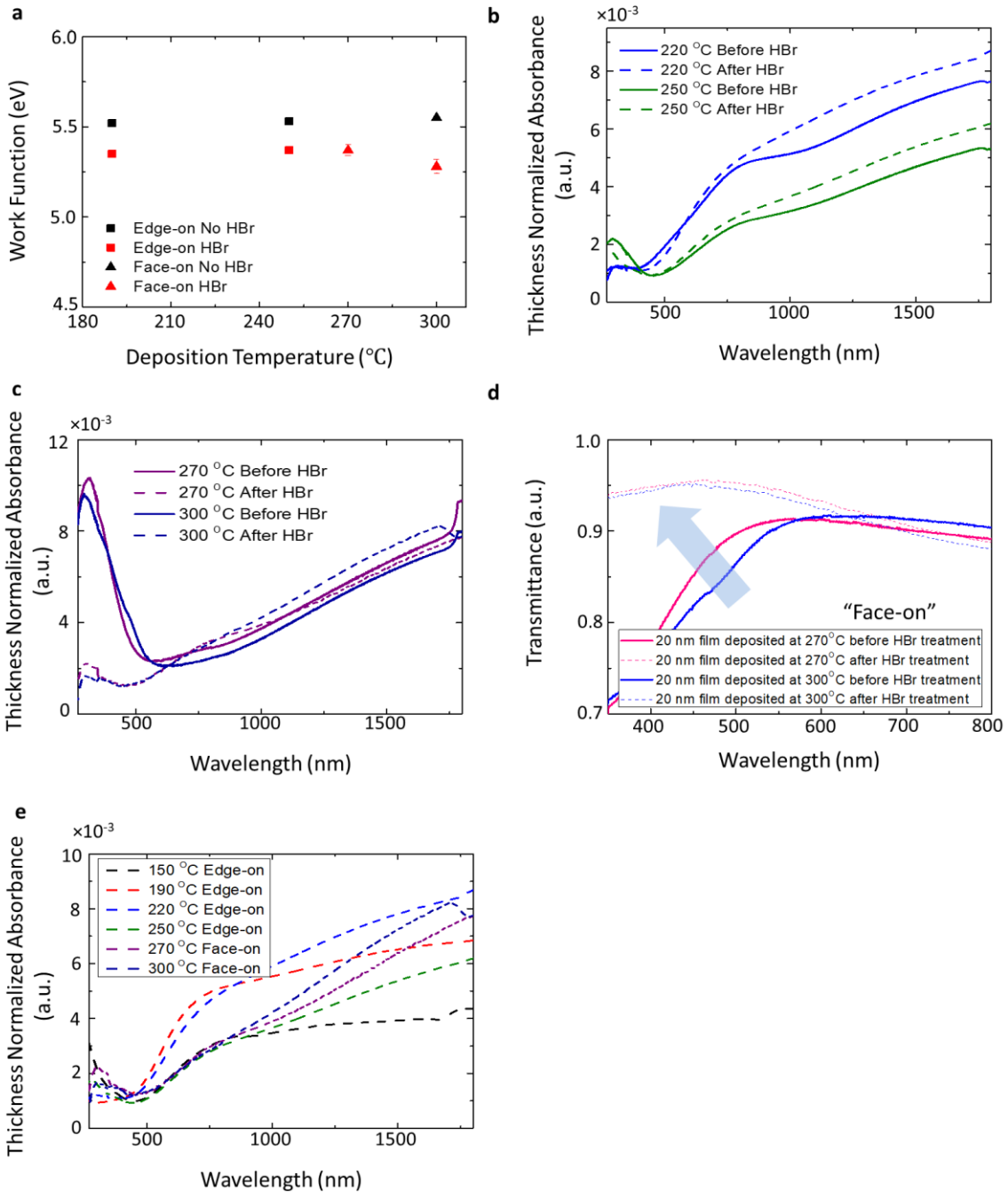

Fig. S12. The effect of HBr rinsing on work function and optical properties. (**a**). The work function of "edge-on" and "face-on" samples deposited at different temperatures before and after HBr treatment. In general, HBr treatment decreases the work function from ~5.5 eV to ~5.3 eV. (**b**). The thickness normalized UV-vis-NIR spectra of "edge-on" PEDOT thin films before and after HBr treatment. The samples are deposited at 220°C and 250°C respectively. (**c**). The thickness normalized UV-vis-NIR spectra of "face-on" PEDOT thin films before and after HBr treatment. (**d**). Transmittance of the "face-on" films. In the visible range (390 -700 nm), the transmittance is much improved by HBr rinsing in "face-on" films. (**e**). The thickness normalized UV-vis-NIR spectra of various PEDOT thin films deposited at different temperatures after HBr treatment.

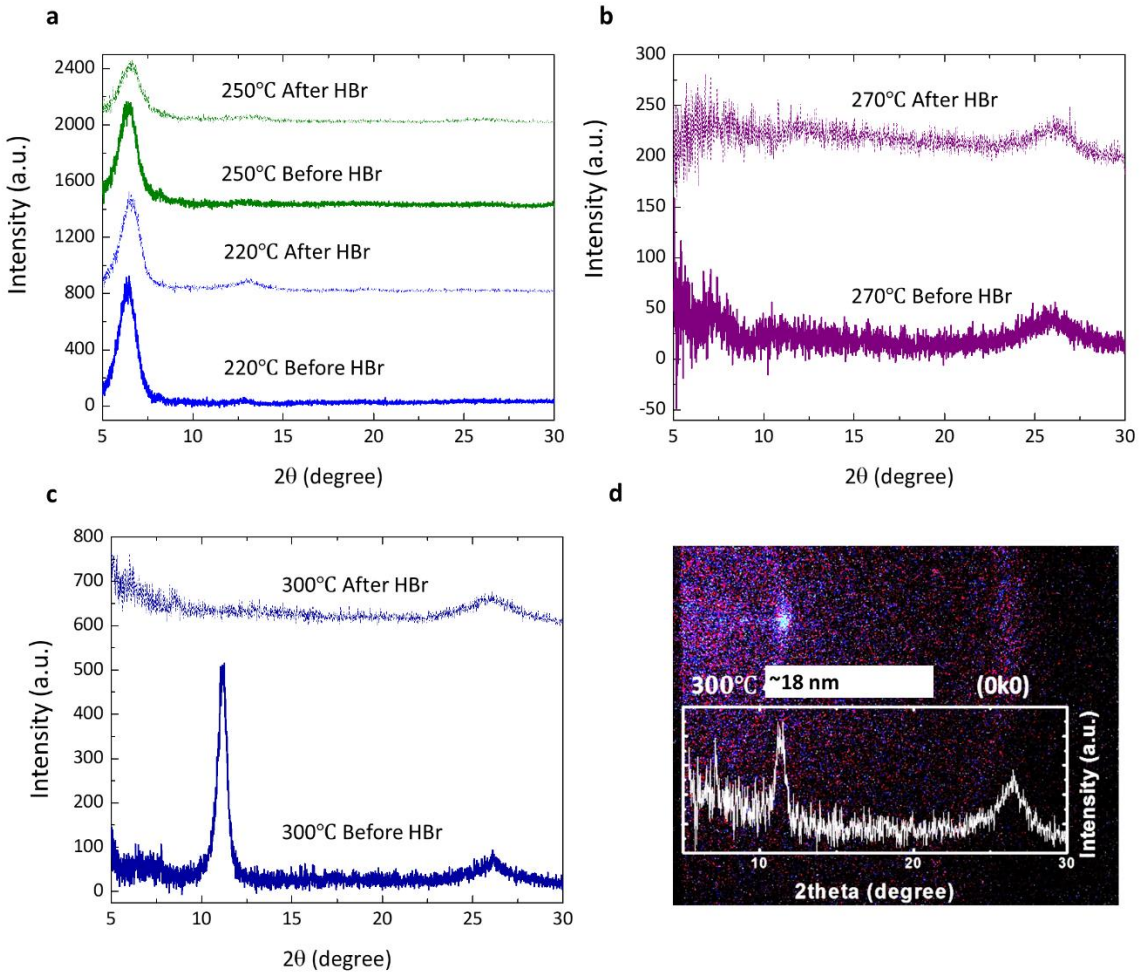

Fig. S13. The effect of HBr rinsing on crystallization. (**a**). The XRD results showing that the HBr treatment does not affect the stacking fashion significantly for "edge-on" samples. The peak intensity is decreased by HBr treatment. This may be due to the disturbance of the lattice by increased effective carrier density. (**b**). The XRD results showing that the HBr treatment does not affect the stacking fashion significantly for "face-on" samples. (**c**). The XRD results showing that the HBr treatment does not affect the stacking fashion significantly for "face-on" samples. In addition, the peak at $2\theta \sim 12^{o}$ corresponds to the peak for the impurity. The HBr treatment can remove impurities in the high temperature grown polymer thin films. (**d**). The XRD map (θ–2θ) of the 18 nm "face-on" film deposited at 300°C before HBr treatment. Comparing with the HBr treated XRD shown in Figure 1c, we observe that HBr treatment has the effect to remove the impurity.

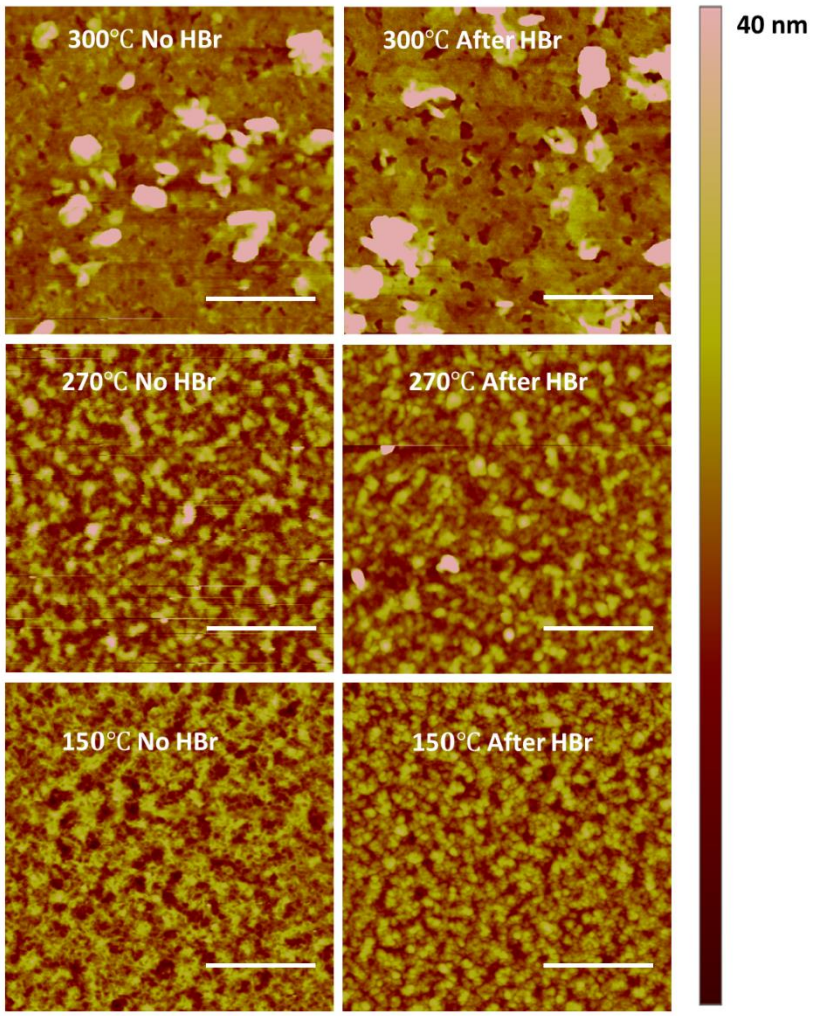

Fig. S14. The effect of HBr rinsing on surface morphology of PEDOT thin films. AFM images of PEDOT thin films deposited at 150°C (30 nm, "edge-on" stacking), 270°C (12 nm, "face-on" stacking), and 300°C (10 nm, "face-on" stacking), before and after HBr treatment, are shown here. The scale bar is 1 μm. HBr treatment does not change the morphology significantly.

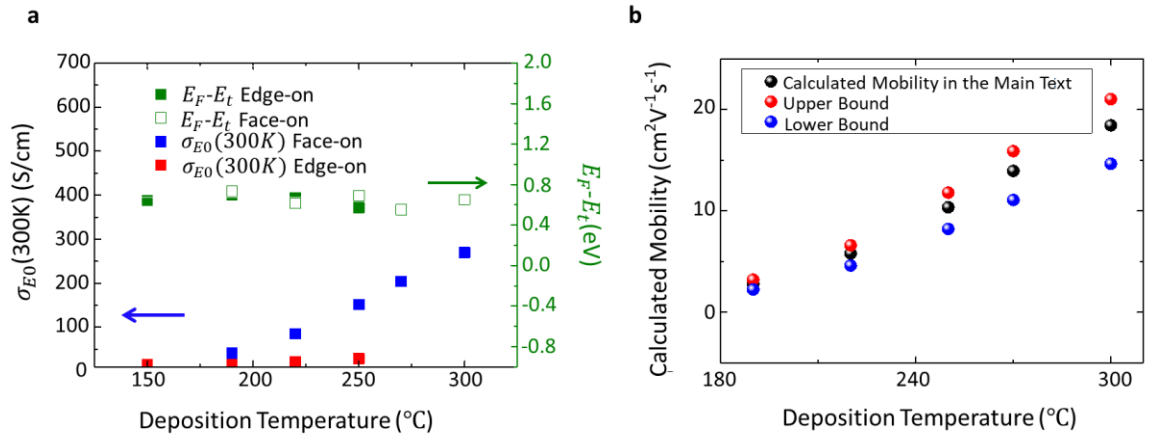

Fig. S15. Calculated $E_F - E_t$ and the sensitivity analysis of the Seebeck coefficient measurement error on the calculated carrier mobility. (**a**). Left y-axis: calculated transport coefficient σ_{E0} at 300 K. Right y-axis: calculated $E_F - E_t$ using the Seebeck coefficient measured. (**b**). The upper bound and the lower bound of the carrier mobility caused by the error induced by Seebeck coefficient measurement are shown as the red and blue dots respectively.

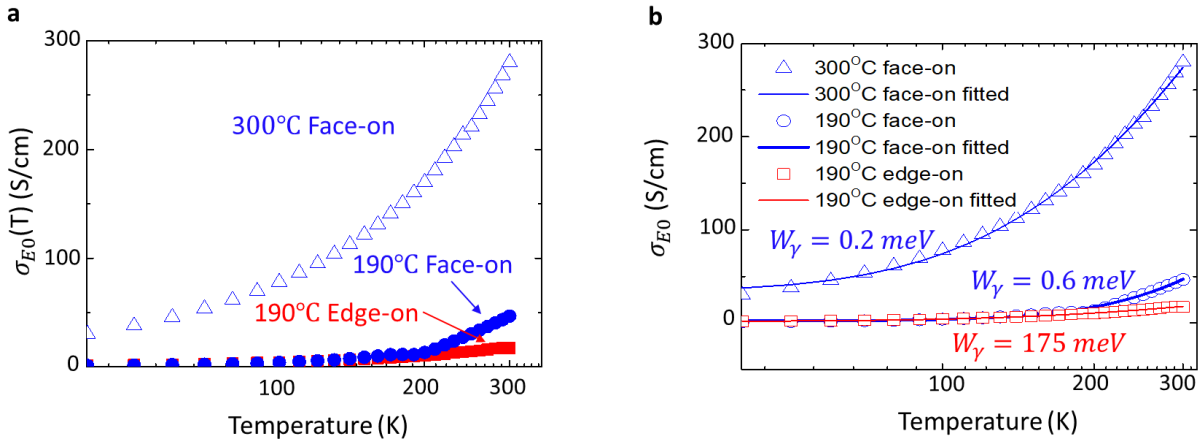

Fig. S16. Extracting the energy barrier of intercrystallite charge carrier transport. (**a**). the σ_{E0} as a function of measurement temperature for three samples. (**b**). the fitting result using σ_{E0} data.

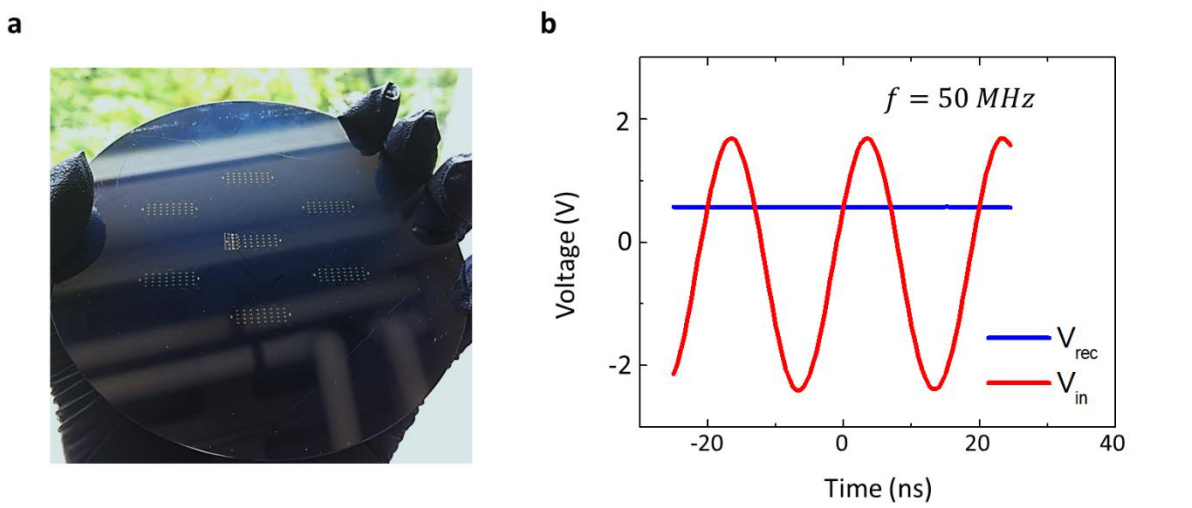

Fig. S17. Wafer-scale fabrication of the RF rectifier arrays. (**a**). the photograph showing the wafer scale RF rectifier arrays. (**b**). The performance of the rectifier at 50 MHz. Photo credit: Xiaoxue Wang, Massachusetts Institute of Technology